
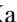
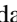





ALMA Reveals a Cloud–Cloud Collision that Triggers Star Formation in the Small Magellanic Cloud

Naslim Neelamkodan¹ , Kazuki Tokuda^{2,3} , Susmita Barman⁴, Hiroshi Kondo², Hidetoshi Sano³ , and Toshikazu Onishi² 

¹Department of Physics, United Arab Emirates University, Al-Ain, 15551, UAE; naslim.n@uaeu.ac.ae

²Department of Physical Science, Graduate School of Science, Osaka Prefecture University, 1-1 Gakuen-cho, Sakai, Osaka 599-8531, Japan

³National Astronomical Observatory of Japan, National Institutes of Natural Science, 2-21-1 Osawa, Mitaka, Tokyo 181-8588, Japan

⁴School of Physics, University of Hyderabad, Prof. C. R. Rao Road, Gachibowli, Telangana, Hyderabad, 500046, India

Received 2020 December 14; revised 2021 January 11; accepted 2021 January 21; published 2021 February 23

Abstract

We present the results of Atacama Large Millimeter/submillimeter Array observations in $^{12}\text{CO}(1-0)$ emission at $0.58 \times 0.52 \text{ pc}^2$ resolution toward the brightest H II region N66 of the Small Magellanic Cloud (SMC). The $^{12}\text{CO}(1-0)$ emission toward the north of N66 reveals clumpy filaments with multiple velocity components. Our analysis shows that a blueshifted filament at a velocity range of $154.4\text{--}158.6 \text{ km s}^{-1}$ interacts with a redshifted filament at a velocity of $158.0\text{--}161.8 \text{ km s}^{-1}$. A third velocity component at a velocity range of $161\text{--}165.0 \text{ km s}^{-1}$ constitutes hub-filaments. An intermediate-mass young stellar object (YSO) and a young pre-main-sequence star cluster have hitherto been reported in the intersection of these filaments. We find a V-shape distribution in the position–velocity diagram at the intersection of two filaments. This indicates the physical association of those filaments due to a cloud–cloud collision. We determine the collision timescale $\sim 0.2 \text{ Myr}$ using the relative velocity ($\sim 5.1 \text{ km s}^{-1}$) and displacement ($\sim 1.1 \text{ pc}$) of those interacting filaments. These results suggest that the event occurred about 0.2 Myr ago and triggered the star formation, possibly an intermediate-mass YSO. We report the first observational evidence for a cloud–cloud collision that triggers star formation in N66N of the low metallicity $\sim 0.2 Z_{\odot}$ galaxy, the SMC, with similar kinematics as in N159W–South and N159E of the Large Magellanic Cloud.

Unified Astronomy Thesaurus concepts: [Star formation \(1569\)](#); [Small Magellanic Cloud \(1468\)](#); [Interstellar medium \(847\)](#); [H II regions \(694\)](#)

1. Introduction

Massive stars significantly influence the dynamics and physical conditions of the interstellar medium and play a key role in galaxy evolution. It is, therefore, essential to understand the fundamental physical processes of the parent molecular cloud. These stars are relatively rare because they are short-lived and evolve quickly compared to their low-mass counterparts. They are often found in clusters, and their early formation phase is highly complex due to the influence on the local environment by gravitational collapse and high radiation pressure (Zinnecker & Yorke 2007; Motte et al. 2018). The triggered star formation at the shock-compressed layers of two colliding clouds is suggested to be a possible way to induce the formation of massive stars in a cluster environment (Inoue & Fukui 2013). Recent advances in molecular line observations have revealed evidence for the cloud–cloud collision that triggers the formation of massive cloud cores and stars in the Galactic clouds (e.g., Dobashi et al. 2014; Torii et al. 2015, 2017; Fukui et al. 2016, 2018a, 2018b). Observations with Atacama Large Millimeter Array (ALMA) have allowed us to extend these findings to the extragalactic clouds. These include N159W–South and N159E in the Large Magellanic Cloud (LMC; Fukui et al. 2015, 2019; Tokuda et al. 2019), and some evident star-forming regions in M33 (Muraoka et al. 2020; Sano et al. 2021; Tokuda et al. 2020).

The Small Magellanic Cloud (SMC) galaxy is an excellent laboratory to study the high-mass star-forming regions in the low metallicity at a subparsec resolution due to its close proximity (61 kpc; Hilditch et al. 2005) and low metallicity ($0.1\text{--}0.2 Z_{\odot}$; Russell & Dopita 1992; Rolleston et al. 2003; Lee et al. 2005). The star-forming region N66 is the largest and the most luminous H II region in the SMC, which comprises a variety of stellar

populations, including young stellar objects (YSO), as well as pre-main-sequence (PMS) and main-sequence OB star association. The region hosts nearly 33 OB stars, that is about half of the entire SMC hot star population (Massey et al. 1989; Walborn et al. 2000; Evans et al. 2006). The majority of this massive star population is located in the central bar of the nebula that appears as a well-defined arc structure extending from southeast to northwest in an H α map (Figure 1). These stars are major sources of photoionization in the central bar of N66 that can effectively trigger star formation via stellar wind and shock (Elmegreen & Lada 1977). A study of gas and dust content of the N66 by Rubio et al. (2000) shows a tight correlation of H $_2$ emission with CO and infrared aromatic emission. The CO has been largely photodissociated by far-ultraviolet (FUV) radiation from nearby massive stars in both the central bar and northern filament. Similar characteristics of photodissociation regions are reported in many Galactic and extragalactic clouds (Tielens et al. 1993; Roussel et al. 2007; Naslim et al. 2015). N66 is, therefore, the most appropriate target to investigate the high-mass star formation mechanism in the SMC.

The deep imaging survey with the Hubble Space Telescope shows that the region harbors at least five clusters of low-mass PMS stars with a significant age difference (Hennekemper et al. 2008). These include the stellar population of age $\leq 5 \text{ Myr}$, and those with age $\leq 10 \text{ Myr}$. Two PMS star clusters in the north of N66 central bar are younger ($\leq 2.5 \text{ Myr}$) than those in the bar, suggesting that these clusters are formed after the central bar population by a different formation mechanism (Hennekemper et al. 2008). Sewilo et al. (2013) have reported many high-mass and intermediate-mass YSOs in N66. Rubio et al. (2000) have indicated the presence of infrared emission peaks both in the central bar and the north of N66 that coincides with the young

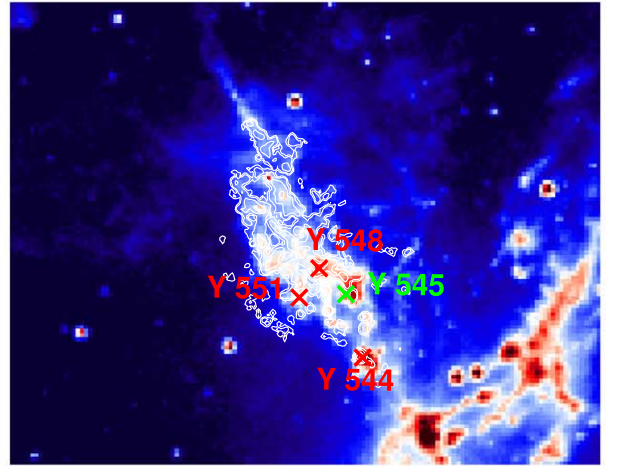
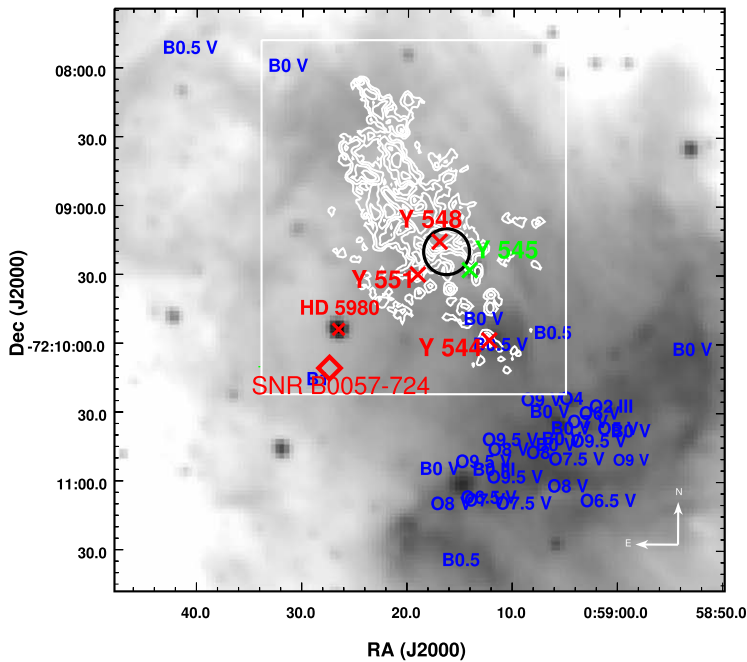


Figure 1. Left: the $H\alpha$ map of N66 is shown along with $^{12}\text{CO}(1-0)$ emission (contour) of N66N. The white box shows the region N66N of this study. The OB stars, SNR B0057-724, and four YSOs close to the $^{12}\text{CO}(1-0)$ filaments are labeled. The location of PMS star cluster 2 (Hennekemper et al. 2008) is shown (black circle) for comparison. Right: Spitzer $8.0\ \mu\text{m}$ map of N66N is shown along with $^{12}\text{CO}(1-0)$ emission in contour.

stellar population identified by Sewilo et al. (2013). Possible sequential star formation due to the photodissociation by OB star association in the central bar has been suggested (Rubio et al. 2000). However, the mechanism for forming a relatively younger population in the north of N66 is debated.

In this Letter, we present the first results of the ALMA observation of $^{12}\text{CO}(1-0)$ toward the northern filaments of N66 (N66N) in the SMC.

2. Observations/Data

We used the ALMA archival data (P.I., Erik Muller, #2015.1.01296.S) of the N66N. The Band 3 (3 mm) observations were performed using the 12 m array with the configurations of C36-1/2, C36-2/3, and C40-6 during the Cycle 3 and 4 observing seasons. The representative spectral window targeted the $^{12}\text{CO}(J=1-0)$ line with a frequency resolution of 61 kHz and a channel number of 3840. We performed the imaging process using the Common Astronomy Software Application (CASA) package (McMullin et al. 2007) version 5.4.1. The weighting scheme of the `tclean` was “Briggs” with a robust parameter of 0.5. The `auto-multithresh` procedure (Kepley et al. 2020) automatically selected the emission mask in the dirty and residual images in `tclean`. We continued the deconvolution process until the intensity of the residual image attained the $\sim 1\sigma$ noise level. The resultant beam size and rms noise level are $2''.0 \times 1''.8$ (P.A. = 10° ; $0.58 \times 0.52\ \text{pc}^2$) and $0.022\ \text{Jy beam}^{-1}$ ($=0.59\ \text{K}$) at a velocity resolution of $0.2\ \text{km s}^{-1}$, respectively.

To investigate the missing flux of the 12 m array data, we retrieved another ALMA program (P.I., Claudia, Agliozzo, #2017.A.00054.S), which contains the Atacama Compact Array (ACA) 7 m array data alone in $^{12}\text{CO}(J=1-0)$ toward the N66 region. We applied the same flow described in the previous paragraph to the data reduction (imaging) process. We converted the 12 m array data to be the same resolution as the 7 m array data, and then produced the integrated intensity ratio map in the pixels

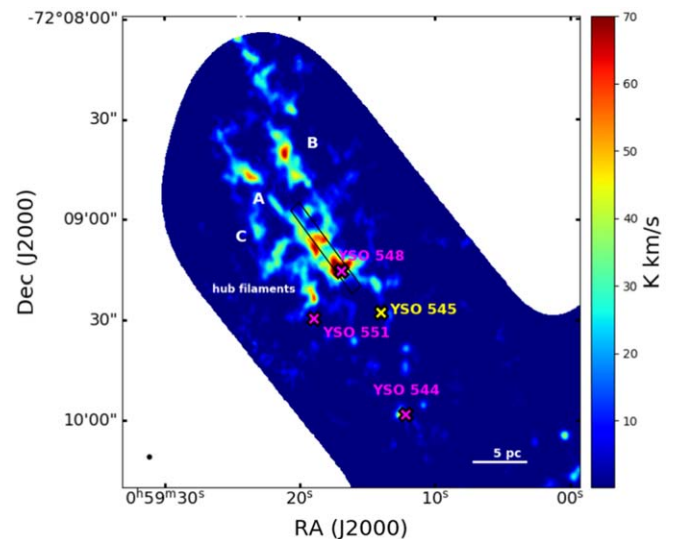


Figure 2. The $^{12}\text{CO}(1-0)$ integrated intensity map of N66N. Filaments A, B, and C, and the positions of YSOs are labeled for comparison. The angular resolution $2''.0 \times 1''.8$ is shown (black ellipse) in the left bottom corner.

at a more than 3σ detection. Since the flux ratio between the two data sets is almost 1, we conclude that the 12 m array data does not suffer from the significant missing flux. We used the 12 m array data throughout this manuscript.

3. Results

3.1. $^{12}\text{CO}(1-0)$ Spatial Distributions and Filaments

Figure 2 shows the velocity integrated intensity distribution of $^{12}\text{CO}(1-0)$ emission, which reveals the filamentary and clumpy structures of N66N. Two well-ordered filaments (A and B) appear as elongated structures extending from the dense clumps toward the northeast of N66 (Figure 2). There is a third

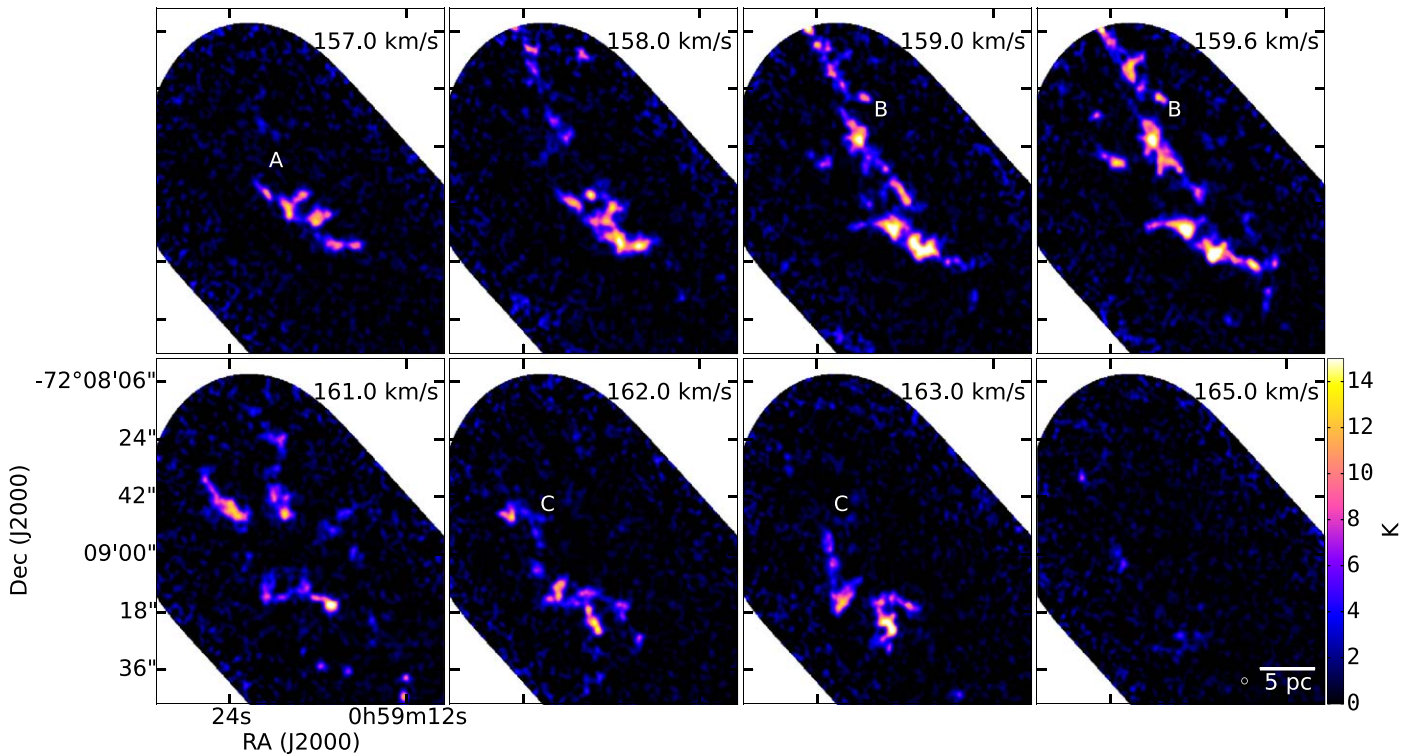


Figure 3. The $^{12}\text{CO}(1-0)$ velocity channel maps toward the N66N. The velocity is given in the upper right corner of each panel. The angular resolution $2''.0 \times 1''.8$ is shown in the right bottom corner.

filamentary structure that constitutes multiple small filaments, similar to the structures indicated as hub-filaments in many other high-mass star-forming regions (Peretto et al. 2013; Motte et al. 2018; Tokuda et al. 2019; Kumar et al. 2020). In Figure 1, we show the distribution of $^{12}\text{CO}(1-0)$ emission in N66N on an $\text{H}\alpha$ map (Smith & MCELS Team 1998), and the Spitzer $8.0 \mu\text{m}$ map (Gordon et al. 2011). For comparison, we show the location of four YSOs closer to the N66N and 41 OB stars (Dufton et al. 2019) that distribute over the entire N66. The ionized gas traced by $\text{H}\alpha$ emission shows a giant H II region in the center of N66 that appears as a bar. Toward the N66N filamentary complex, the $\text{H}\alpha$ emission appears to be more diffuse. To the southwest of the $^{12}\text{CO}(1-0)$ filaments, there exists a compact $\text{H}\alpha$ emission complex. The distribution of $8.0 \mu\text{m}$ emission in N66N shows multiple filaments, and the morphology resembles the spatial distribution of $^{12}\text{CO}(1-0)$ emission.

To estimate the filament’s mass and size, we identify the filament structures using the python package *astrodendro* (Rosolowsky et al. 2008). *astrodendro* characterizes the molecular gas as a structure tree with leaves, branches, and trunks in a three-dimensional data cube. The trunk represents the parent cloud, which constitutes the brightest structures as leaves, and the low-density connecting structures as branches. We identify the filaments as the parent structures that are the trunks in the dendrogram. *astrodendro* provides basic parameters such as size, velocity dispersion, and flux of molecular structures. We obtain the length and width of the filaments, A and B, from the respective major and minor axes of the trunks (σ_x, σ_y). We derive the apparent velocity width of each filament using the velocity dispersion, σ_v , assuming a Gaussian distribution ($\Delta V = 2\sqrt{2 \ln 2} \sigma_v$). The derived velocity dispersion of filament A is 0.7 km s^{-1} that corresponds to a velocity width

of 1.7 km s^{-1} . The length and width of filament A are 13 pc and 3.8 pc, respectively. Assuming a CO- H_2 conversion factor of $7.5 \times 10^{20} \text{ cm}^{-2} (\text{K km s}^{-1})^{-1}$ for the SMC (Muraoka et al. 2017), we find an H_2 column density of $3.2 \times 10^{22} \text{ cm}^{-2}$ for filament A that translates to an average mass of $\sim 2.3 \times 10^3 M_\odot$. Filament B shows a velocity dispersion of 0.88 km s^{-1} ($\Delta V = 2.1 \text{ km s}^{-1}$) with a length of ~ 21 pc and width of ~ 3 pc. The H_2 column density of filament B is estimated to be $5.8 \times 10^{22} \text{ cm}^{-2}$ with a mass of $\sim 4.3 \times 10^3 M_\odot$.

3.2. Velocity Structures

The complexity of velocity structures is visible in a series of channel maps (Figure 3). The molecular cloud has an elongated filamentary structure that is spread over a velocity range of $154.4\text{--}165.2 \text{ km s}^{-1}$. Filament A shows a velocity range of $154.4\text{--}158.6 \text{ km s}^{-1}$ and filament B shows a velocity range of $158.0\text{--}161.8 \text{ km s}^{-1}$. We find a third velocity component (Filament C) in a velocity range of $161\text{--}165.0 \text{ km s}^{-1}$.

Figure 4(a) shows the first-moment intensity weighted velocity (moment 1) map of $^{12}\text{CO}(1-0)$ emission in N66N. The moment 1 map reveals the blueshifted and redshifted velocity components (A and B) relative to the systemic velocity $\sim 158 \text{ km s}^{-1}$. In Figure 4(b), we show the three velocity components in $^{12}\text{CO}(1-0)$ integrated intensity contours. The blue contour represents the blueshifted filament A with the peak emission at a velocity of 157.4 km s^{-1} and the green contour represents the redshifted filament B with a velocity peak at 160 km s^{-1} . The red represents the redshifted third component C at a peak velocity of 163 km s^{-1} .

The position–velocity (PV) diagram at the intersection of filaments A and B shows a V-shaped gas distribution (Figure 5), indicating the physical connection of two filaments. This V-shape gas distribution at the filament intersection in the PV diagram is a

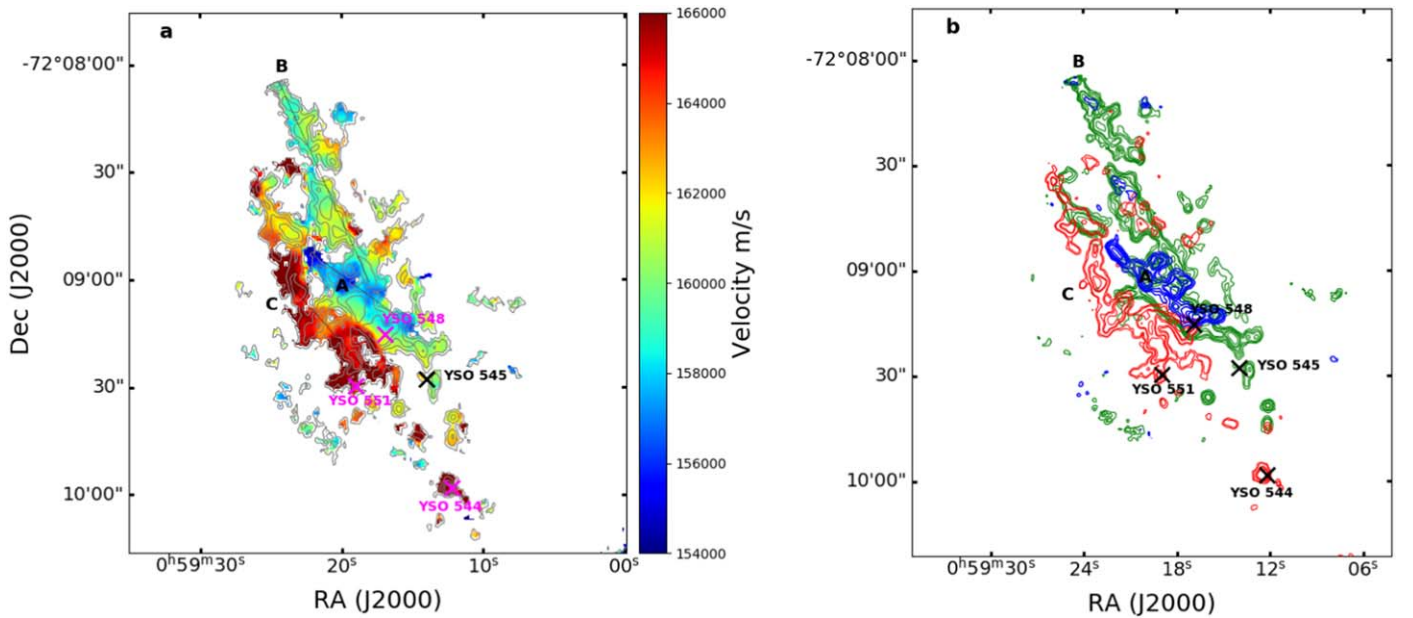


Figure 4. Panel (a): the $^{12}\text{CO}(1-0)$ first-moment intensity weighted velocity map of N66N. Panel (b): the blueshifted component A (blue), the second velocity component B (green), and the third redshifted component C (red) are shown in $^{12}\text{CO}(1-0)$ integrated intensity contours. The contour levels are 3, 20, 30, and 60 K km s^{-1} .

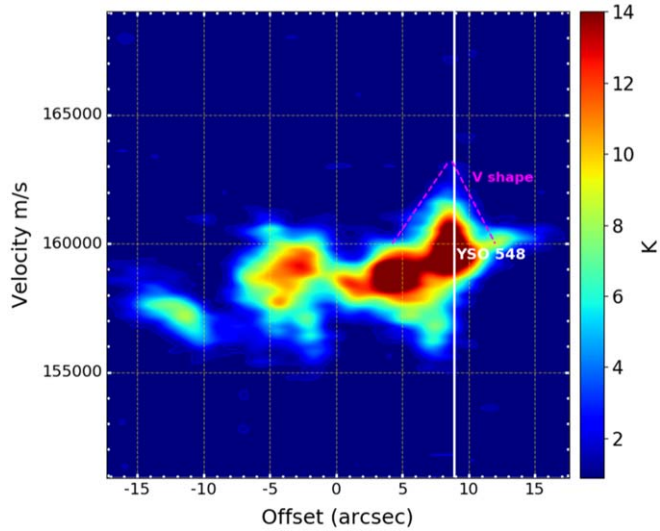


Figure 5. The V-shape distribution in a position–velocity diagram at the intersection of filaments A and B across the cut shown in Figure 2. The position of YSO 548 along the V-shape is labeled.

key observational signature of the cloud–cloud collision (see the discussion in Section 5).

4. CO Cores in Filaments and Associated Young Stellar Population

The velocity integrated $^{12}\text{CO}(1-0)$ intensity map of N66N shows localized emission peaks along the filaments. We use *astrodendro* to identify the molecular cores and determine their virial masses, following the same method as in Naslim et al. (2018) and Nayana et al. (2020). We identify the molecular cores as the dendrogram leaves, which are the brightest and smallest structures representing the top level of the dendrogram. We detect three CO cores along filament A that show the virial masses 19, 350, and $1300 M_{\odot}$, and the total

of nine CO cores along the filament B in a mass range of $120\text{--}565 M_{\odot}$. There are 16 CO cores in the third velocity component C in a mass range of $20\text{--}225 M_{\odot}$. We note three molecular cores at the intersection of A and B with virial masses of 156, 173, and $1442 M_{\odot}$.

To investigate the ongoing star formation in N66N, we adopt the YSOs identified by Sewilo et al. (2013). Figures 2 and 4 show the positions of three highly reliable YSOs (548, 551, and 544) and one less reliable YSO (545).

5. Discussion

Observations of molecular clouds in the Milky Way and the LMC have shown that filaments of different velocities can be a result of colliding clouds triggering high-mass star formation. To find proper evidence for a cloud–cloud collision, we use three methods discussed by Fukui et al. (2018a). (a) Velocity distribution of molecular gas in channel maps: we find multiple velocity components in channel maps. One filament at a blueshifted velocity gradient $154.4\text{--}158.6 \text{ km s}^{-1}$ (filament A) seems to interact with a redshifted filament of velocity $158.0\text{--}161.8 \text{ km s}^{-1}$ (filament B). Multiple hub-filaments are found in a third redshifted component at a velocity range of $161\text{--}165.0 \text{ km s}^{-1}$. (b) Velocity distribution in a first-moment map: three velocity components are found. A YSO has been reported at the intersection (Sewilo et al. 2013). A similar filament distribution is reported in N159E of the LMC (Saigo et al. 2017; Fukui et al. 2019). (c) Position–velocity diagram: we find a V-shape gas distribution at the intersection of filaments A and B, indicating their physical interaction. These observational signatures are consistent with the cloud–cloud collision reported in N159W-South, N159E of the LMC, and NGC 604 of M33 (Fukui et al. 2019; Tokuda et al. 2019; Muraoka et al. 2020).

N159W-South region of the LMC shows complex filaments with multiple velocities and a V-shape distribution in the PV diagram (Tokuda et al. 2019). The formation of such

complicated filamentary structures and the massive YSOs at the intersection is suggested to be due to the large-scale colliding flow. At a distance of 50 pc away from N159W-South, the N159E star-forming region shows similar filamentary characteristics with multiple velocity components and a massive YSO at the intersection (Saigo et al. 2017). Using a higher spatial-resolution observation, Fukui et al. (2019) reveal more than a few tens of filamentary structures and the protostar activities at the filament intersection. The orientation of these multiple filaments follows a large-scale HI flow, which is driven by the tidal interaction between the SMC and the LMC. Comparing these observations with the magnetohydrodynamic (MHD) numerical simulation (Inoue et al. 2018), Fukui et al. (2019) suggest that the formation of filaments and protostars is a result of HI colliding flow. Muraoka et al. (2020) claim a similar large-scale colliding flow as a potential cause for the formation of multiple filaments and protostars in the NGC 604 cloud of M33. McClure-Griffiths et al. (2018) report the large-scale HI outflows extending about 2 kiloparsecs from the SMC bar, which can be driven by the tidal/ram pressure interaction between the SMC and the LMC. The collision in N66N may be a part of this HI outflow. McClure-Griffiths et al. (2018) do not provide any evidence for the return of this HI flow into the SMC. To further explain whether the collision in N66N is related to a large-scale flow, we need to study the velocity structure of HI gas.

The MHD numerical simulation of two colliding clouds of different sizes have shown the formation of a shock-compressed layer between two clouds (Inoue & Fukui 2013). The density and turbulent velocity are enhanced in the shock-compressed interface due to an amplified magnetic field, and the magnetohydrodynamical fluid flow induces the formation of filaments in multiple velocities (Inoue & Fukui 2013). The MHD simulations by Inoue et al. (2018) claim that the massive filaments are formed in the shock-compressed layer between the cloud and a large-scale gas flow. If the actual line mass exceeds the critical value, the filaments become gravitationally unstable and further collapse into fragments and form molecular cores. The mass accretion creates multiple dense cores at the intersection, where the most massive core becomes an O star accompanied by several low-mass stars. Since the colliding cloud is very massive ($>50 M_{\odot}$), the mass accretion rate onto the central cloud can be as large as $\sim 10^{-4} M_{\odot} \text{yr}^{-1}$. This leads to the formation of massive cores as large as $\sim 100 M_{\odot}$ in 0.3 Myr (Inoue & Fukui 2013; Fukui et al. 2016). We estimate the timescale of cloud collision in N66N using the relative displacement and velocity of two interacting filaments. The displacement between two filaments on their relative location at the point of intersection is estimated to be 0.8 pc with a relative velocity of 3.6 km s^{-1} . If we assume the relative motion of colliding clouds has an angle of 45° to the line of sight, we get a projection corrected velocity of $\sim 5.1 \text{ km s}^{-1}$ and a displacement of $\sim 1.1 \text{ pc}$. We estimate the collision timescale to be $\sim 0.2 \text{ Myr}$. Three $^{12}\text{CO}(1-0)$ cores in a mass range of $156-1442 M_{\odot}$ are identified at the filament intersection. High column density is an essential initial condition for forming high-mass stars by cloud–cloud collision. A peak column density of $\sim 10^{23} \text{ cm}^{-2}$ can produce nearly 10 O stars, while a single O star can be produced with a peak column density of $\sim 10^{22} \text{ cm}^{-2}$ (Fukui et al. 2016). The H_2 column densities of two interacting filaments in N66N are $3.2 \times 10^{22} \text{ cm}^{-2}$ and $5.8 \times 10^{22} \text{ cm}^{-2}$.

The young stellar population and massive star content of N66 have been extensively studied (Massey et al. 1989; Sewilo et al. 2013). To investigate the ongoing star formation, we compare the positions of YSOs (Sewilo et al. 2013) and OB stars (Dufton et al. 2019) with the CO cores in filaments. We find that the majority of OB stars and YSOs are in the N66 central bar, and four YSOs (548, 551, 544, and 545) are located in the northeast. Among these, the most reliable YSO 548 is at the filament intersection and YSO 551 is in a hub-filament. The YSO 544 is in a compact H II region between the filament intersection and the central bar. We do not have enough parametric information such as the mass and luminosity of YSO 548. Sewilo et al. (2013) provide an $8.0 \mu\text{m}$ magnitude of [10.69] for YSO 548, indicating an intermediate-mass (mass range $5-10 M_{\odot}$) object according to the selection criterion suggested by Chen et al. (2009). The YSO 548 is associated with a ^{12}CO core of virial mass $156 M_{\odot}$. It is also possible that a massive YSO remains to be formed in the densest core at the intersection. Sewilo et al. (2013) report a mass of $\sim 10.1 M_{\odot}$ and a luminosity of $3.24 \times 10^3 L_{\odot}$ for YSO 544. The ^{12}CO core associated with YSO 544 shows a virial mass of $\sim 398 M_{\odot}$, although there is no extended CO emission.

The $^{12}\text{CO}(1-0)$ filaments in N66N have similar morphology with the $8.0 \mu\text{m}$ emission, indicating the photoelectric heating of polycyclic aromatic hydrocarbon by FUV radiation, possibly from OB stars in the central bar. The extended low-density H α emission and $^{12}\text{CO}(1-0)$ filaments in N66N show a vertical orientation with the H II region in the central bar. Ye et al. (1991) suggest a high-velocity ‘‘Champagne flow’’ from the exciting OB stars in the central bar toward the northeast. The H II region in the central bar are photodissociating the natal molecular clouds, but some of the clouds are still surviving at N66N where the cloud collision seems to be taking place, resulting in a formation of at least an intermediate-mass star at the intersection of two filaments. In addition to the YSO 548, a PMS star cluster is located in the filament intersection. This PMS star cluster is a relatively younger population (0.25–2.5 Myr) than those in the central bar (0.5–10 Myr; Hennekemper et al. 2008) and located 24 pc away from the central bar in the filament intersection. We expect this low-mass PMS cluster has been formed prior to the cloud–cloud collision as it is found to be slightly older than the estimated collision timescale $\sim 0.2 \text{ Myr}$. Gouliermis et al. (2008) have proposed that this PMS population outside of the central bar can be triggered by the wind-driven expanding H II region blown by the supernova remnant SNR B0057-724 (Ye et al. 1991; Nazé et al. 2002) (Figure 1), which is in the east of the filament intersection at a projected distance of $\sim 21 \text{ pc}$. Although the redshifted filament C has an overlap with an edge of the X-ray emission (Nazé et al. 2002), we do not find a continuous velocity gradient with an expanding shell of molecular gas that is blown from SNR B0057-724 in the direction of filament intersection.

We finally remark on star formation in the SMC-like low-metallicity environment ($0.1-0.2 Z_{\odot}$) and the future prospect of this study. The numerical simulations by Ricotti et al. (1997) and Ricotti & Ferrara (2002) show that the kinetic energy dissipation of the cloud collision decreases in a lower-metallicity condition due to the longer cooling timescale of the shocked gas than the characteristic collision time; hence a significant effect on the star formation is expected. Our finding indicates that cloud–cloud collision does occur and works as a

trigger of star formation in low-metallicity environment. However, the N66N region hosts several YSOs, such as YSO 544, associated with a compact/isolated CO clump, which is not evident in more than two velocity components at the current angular resolution. The subsequent step is to understand how common the cloud–cloud collision throughout the N66 region and the SMC, and how the properties of parental molecular clouds affect the mass and luminosity of embedded YSO. A more comprehensive analysis extending to the other YSOs using the current data set in N66 will be presented in a future paper.

6. Conclusion

We report clumpy filaments with multiple velocity components toward N66N in the SMC by ALMA. Our results are concluded as follows:

1. The ALMA observation of $^{12}\text{CO}(1-0)$ emission in N66N shows a blueshifted velocity component (A) in a velocity range of $154.4-158.6 \text{ km s}^{-1}$ and a redshifted component (B) in a velocity range of $158.0-161.8 \text{ km s}^{-1}$. A third redshifted component (C) in a velocity range of $161-165.0 \text{ km s}^{-1}$ shows hub-filament distribution.
2. An intermediate-mass YSO has been found at the intersection of filaments A and B. We find a V-shape gas distribution in the PV diagram taken at the intersection of filaments A and B, indicating their physical association. These filament characteristics are similar to the cloud–cloud collision reported in N159E of the LMC.
3. We find the H_2 column densities of two interacting filaments using a CO-to- H_2 conversion factor of $7.5 \times 10^{20} \text{ cm}^{-2} (\text{K km s}^{-1})^{-1}$. The redshifted component has an H_2 column density of $5.8 \times 10^{22} \text{ cm}^{-2}$ and mass $\sim 4.3 \times 10^3 M_{\odot}$, while the blueshifted component shows a column density $3.2 \times 10^{22} \text{ cm}^{-2}$ and mass $\sim 2.3 \times 10^3 M_{\odot}$.
4. We estimate the timescale of collision $\sim 0.2 \text{ Myr}$ using the relative velocity $\sim 5.1 \text{ km s}^{-1}$ and displacement $\sim 1.1 \text{ pc}$ of two interacting filaments.
5. Comparing our findings with the results of MHD simulations (Inoue et al. 2018), molecular line observations in N159W-South and N159E of the LMC (Fukui et al. 2019) and the NGC 604 of M33 (Muraoka et al. 2020), a cloud collision is a possible triggering mechanism for star formation in N66N. Our results suggest that the collision occurred $\sim 0.2 \text{ Myr}$ ago, resulting in the formation of filaments with multiple velocity components, and triggered the formation of an intermediate-mass YSO.

This paper makes use of the following ALMA data: ADS/JAO.ALMA # 2015.1.01296.S, 2017.A.00054.S. ALMA is a partnership of the ESO, NSF, NINS, NRC, NSC, and ASIAA. The Joint ALMA Observatory is operated by the ESO, AUI/NRAO, and NAOJ. This research has been supported by United Arab Emirates University, under start-up grant 31S378 and UPAR grant G00003479.

ORCID iDs

Naslim Neelamkodan  <https://orcid.org/0000-0001-8901-7287>
 Kazuki Tokuda  <https://orcid.org/0000-0002-2062-1600>
 Hidetoshi Sano  <https://orcid.org/0000-0003-2062-5692>
 Toshikazu Onishi  <https://orcid.org/0000-0001-7826-3837>

References

- Chen, C. H. R., Chu, Y.-H., Gruendl, R. A., Gordon, K. D., & Heitsch, F. 2009, *ApJ*, **695**, 511
- Dobashi, K., Matsumoto, T., Shimoikura, T., et al. 2014, *ApJ*, **797**, 58
- Dufton, P. L., Evans, C. J., Hunter, I., Lennon, D. J., & Schneider, F. R. N. 2019, *A&A*, **626**, A50
- Elmegreen, B. G., & Lada, C. J. 1977, *ApJ*, **214**, 725
- Evans, C. J., Lennon, D. J., Smartt, S. J., & Trundle, C. 2006, *A&A*, **456**, 623
- Fukui, Y., Harada, R., Tokuda, K., et al. 2015, *ApJL*, **807**, L4
- Fukui, Y., Kohno, M., Yokoyama, K., et al. 2018b, *PASJ*, **70**, S41
- Fukui, Y., Tokuda, K., Saigo, K., et al. 2019, *ApJ*, **886**, 14
- Fukui, Y., Torii, K., Hattori, Y., et al. 2018a, *ApJ*, **859**, 166
- Fukui, Y., Torii, K., Ohama, A., et al. 2016, *ApJ*, **820**, 26
- Gordon, K. D., Meixner, M., Meade, M. R., et al. 2011, *AJ*, **142**, 102
- Gouliermis, D. A., Chu, Y.-H., Henning, T., et al. 2008, *ApJ*, **688**, 1050
- Hennekemper, E., Gouliermis, D. A., Henning, T., Brandner, W., & Dolphin, A. E. 2008, *ApJ*, **672**, 914
- Hilditch, R. W., Howarth, I. D., & Harries, T. J. 2005, *MNRAS*, **357**, 304
- Inoue, T., & Fukui, Y. 2013, *ApJL*, **774**, L31
- Inoue, T., Hennebelle, P., Fukui, Y., et al. 2018, *PASJ*, **70**, S53
- Kepley, A. A., Tsutsumi, T., Brogan, C. L., et al. 2020, *PASP*, **132**, 024505
- Kumar, M. S. N., Palmeirim, P., Arzoumanian, D., & Inutsuka, S. I. 2020, *A&A*, **642**, A87
- Lee, J. K., Rolleston, W. R. J., Dufton, P. L., & Ryans, R. S. I. 2005, *A&A*, **429**, 1025
- Massey, P., Parker, J. W., & Garmany, C. D. 1989, *AJ*, **98**, 1305
- McClure-Griffiths, N. M., Dénes, H., Dickey, J. M., et al. 2018, *NatAs*, **2**, 901
- McMullin, J. P., Waters, B., Schiebel, D., Young, W., & Golap, K. 2007, in ASP Conf. Ser. 376, *Astronomical Data Analysis Software and Systems XVI*, ed. R. A. Shaw et al. (San Francisco, CA: ASP), 127
- Motte, F., Bontemps, S., & Louvet, F. 2018, *ARA&A*, **56**, 41
- Muraoka, K., Homma, A., Onishi, T., et al. 2017, *ApJ*, **844**, 98
- Muraoka, K., Kondo, H., Tokuda, K., et al. 2020, *ApJ*, **903**, 94
- Naslim, N., Kemper, F., Madden, S. C., et al. 2015, *MNRAS*, **446**, 2490
- Naslim, N., Tokuda, K., Onishi, T., et al. 2018, *ApJ*, **853**, 175
- Nayana, A. J., Naslim, N., Onishi, T., et al. 2020, *ApJ*, **902**, 140
- Nazé, Y., Hartwell, J. M., Stevens, I. R., et al. 2002, *ApJ*, **580**, 225
- Peretto, N., Fuller, G. A., Duarte-Cabral, A., et al. 2013, *A&A*, **555**, A112
- Ricotti, M., & Ferrara, A. 2002, *MNRAS*, **334**, 684
- Ricotti, M., Ferrara, A., & Miniati, F. 1997, *ApJ*, **485**, 254
- Rolleston, W. R. J., Venn, K., Tolstoy, E., & Dufton, P. L. 2003, *A&A*, **400**, 21
- Rosolowsky, E. W., Pineda, J. E., Kauffmann, J., & Goodman, A. A. 2008, *ApJ*, **679**, 1338
- Roussel, H., Helou, G., Hollenbach, D. J., et al. 2007, *ApJ*, **669**, 959
- Rubio, M., Contursi, A., Lequeux, J., et al. 2000, *A&A*, **359**, 1139
- Russell, S. C., & Dopita, M. A. 1992, *ApJ*, **384**, 508
- Saigo, K., Onishi, T., Nayak, O., et al. 2017, *ApJ*, **835**, 108
- Sano, H., Tsuge, K., Tokuda, K., et al. 2021, *PASJ*, **73**, S62
- Sewilo, M., Carlson, L. R., Seale, J. P., et al. 2013, *ApJ*, **778**, 15
- Smith, R. C. & MCELS Team 1998, *PASA*, **15**, 163
- Tielens, A. G. G. M., Meixner, M. M., van der Werf, P. P., et al. 1993, *Sci*, **262**, 86
- Tokuda, K., Fukui, Y., Harada, R., et al. 2019, *ApJ*, **886**, 15
- Tokuda, K., Muraoka, K., Kondo, H., et al. 2020, *ApJ*, **896**, 36
- Torii, K., Hasegawa, K., Hattori, Y., et al. 2015, *ApJ*, **806**, 7
- Torii, K., Hattori, Y., Hasegawa, K., et al. 2017, *ApJ*, **835**, 142
- Walborn, N. R., Lennon, D. J., Heap, S. R., et al. 2000, *PASP*, **112**, 1243
- Ye, T., Turtle, A. J., & Kennicutt, R. C., Jr. 1991, *MNRAS*, **249**, 722
- Zinnecker, H., & Yorke, H. W. 2007, *ARA&A*, **45**, 48